J Mater Sci: Mater Med (2011) 22:1303–1319
DOI 10.1007/s10856-011-4307-6

Microstructure and in vitro behaviour of 45S5 bioglass coatings deposited by high velocity suspension flame spraying (HVSFS)

L. Altomare · D. Bellucci · G. Bolelli · B. Bonferroni · V. Cannillo · L. De Nardo · R. Gadow · A. Killinger · L. Lusvarghi · A. Sola · N. Stiegler

Received: 22 December 2009 / Accepted: 25 March 2011 / Published online: 3 April 2011

Abstract The high-velocity suspension flame spraying technique (HVSFS) was employed in order to deposit 45S5 bioactive glass coatings onto titanium substrates, using a suspension of micron-sized glass powders dispersed in a water + isopropanol mixture as feedstock. By modifying the process parameters, five coatings with different thickness and porosity were obtained. The coatings were entirely glassy but exhibited a through-thickness microstructural gradient, as the deposition mechanisms of the glass droplets changed at every torch cycle because of the increase in the system temperature during spraying. After soaking in simulated body fluid, all of the coatings were soon covered by a layer of hydroxyapatite; furthermore, the coatings exhibited no cytotoxicity and human osteosarcoma cells could adhere and proliferate well onto their surfaces. HVSFS-deposited 45S5 bioglass coatings are therefore highly bioactive and have potentials as replacement of conventional hydroxyapatite in order to favour osseointegration of dental and prosthetic implants.

D. Bellucci · G. Bolelli · B. Bonferroni · V. Cannillo (✉) · L. Lusvarghi · A. Sola
Department of Materials and Environmental Engineering, University of Modena and Reggio Emilia, Via Vignolese 905, 41125 Modena, Italy
e-mail: valeria@unimore.it

R. Gadow · A. Killinger · N. Stiegler
Institute for Manufacturing Technologies of Ceramic Components and Composites (IMTCCC), University of Stuttgart, Allmandring 7b, 70569 Stuttgart, Germany

L. Altomare · L. De Nardo
Dipartimento di Chimica, Materiali e Ingegneria Chimica "G. Natta", Politecnico di Milano, Via Mancinelli 7, 20131 Milan, Italy

1 Introduction

Load-bearing orthopaedic prostheses (e.g. hip replacements) are normally made of metallic materials, generally Ti and its alloys, and are coated with hydroxyapatite in order to promote osseointegration [1–5]. Of the various methods available for the application of hydroxyapatite coatings (which include sputtering, pulsed laser deposition, sol–gel processing, laser treatments, electrophoresis, etc.) [6–12], thermal spraying techniques (particularly the plasma spraying technique) are the most industrially widespread ones [3, 5, 12], on account of their high productivity and excellent flexibility (they can be readily adapted to different component sizes and geometries and allow a wide range of process parameters adjustment), and they have the ability to keep the substrate at relatively low temperature (thus avoiding undesirable microstructural alterations and/or thermal distortions).

In thermal spraying techniques, a stream of dry powder is injected in a hot gas jet (a DC thermal plasma jet in the case of plasma spraying): this jet melts the powder particles and drags them towards the substrate to be coated. The molten particles impinge onto the substrate, flatten and solidify, acquiring the typical lamellar or "splat" morphology; the coating therefore consists of many layers of overlapping lamellae, which adhere to one another [13].

However, thermally-sprayed hydroxyapatite coatings are affected by some disadvantages. First of all, hydroxyapatite particles heated inside the thermal spray jet undergo chemical and structural alterations, because of the incongruent melting behaviour of this compound. As the temperature increases, it is first de-hydroxylated, then decomposed to tricalcium-phosphate (TCP) and to tetracalcium-phosphate (TTCP), and eventually melted; CaO may even form if the particle temperature becomes high

enough to vaporise P_2O_5 [12, 14–17]. Additionally, molten hydroxyapatite cannot crystallise during the very fast solidification process of splats and forms an amorphous phase. Therefore, the deposition parameters must be accurately adjusted in order to preserve some unmelted hydroxyapatite at the core of the sprayed particles [12, 14–16]. The retention of unmelted material, however, prevents the complete flattening of the sprayed particles, leading to poor interlamellar cohesion and consequently to poor mechanical strength and low Weibull modulus. This can become problematic for long-term adhesion. Additionally, when highly-crystalline coatings are needed (the degree of crystallinity of hydroxyapatite controls its bioactivity and resorption rate), a post-process heat treatment becomes mandatory [16, 18–21]. Such heat treatment increases the cost and time of the process and, most importantly, it can impair the structural and mechanical properties of the titanium alloy and/or it can cause thermal distortions.

A possible alternative to thermally-sprayed hydroxyapatite, in order to prevent the above-mentioned drawbacks, could be the use of bioactive glass coatings, which have already been devoted some attention (some examples are Refs. [22–27]). Glasses do not generally undergo phase or compositional alterations during thermal spraying, as indicated by various previous experiments [22, 28]. Furthermore, in bulk form, bioactive glasses have been shown to be more bioactive than hydroxyapatite [1, 2], which makes them particularly attractive for the replacement of hydroxyapatite coatings. Sintered bioactive glass components have accordingly found applications for the production of bone-replacement parts in orthopaedic surgery [1, 2, 29], but they cannot be employed in load-bearing applications. This is due to their limited mechanical strength and intrinsic brittleness: they are being mainly adopted in oral surgery, ear surgery and iliac crest restoration [1–3].

In this paper, the properties of 45S5 bioglass coatings deposited using an innovative thermal spraying process, the high-velocity suspension flame spraying (HVSFS) technique [30], were evaluated. The HVSFS technique employs a suitably-modified high velocity oxygen-fuel (HVOF) torch in order to process an axially-injected liquid suspension, instead of using a dry powder feedstock, as it normally happens in conventional thermal spraying. This enables the adoption of very fine (micrometric) particles as feedstock material. Fine particles can bring about several advantages in thermal spraying: most notably, they are easy to melt and produce small, thin splats, which strongly adhere to one another, so that the coatings have high strength [31, 32]. Their use has been restrained, up until now, by their obviously poor flowability in dry form, which is not compatible with conventional powder feeders. This flowability problem is circumvented by dispersing these particles in a liquid suspension.

Previous investigations have already indicated that the HVSFS technique is able to deposit high quality glass coatings [33], much superior to those obtained by the conventional plasma-spraying process [34]. Some preliminary studies on HVSFS-deposited A/W glass coatings have also given promising results [35]. Therefore, this paper is also aiming to improve the limited knowledge on the deposition mechanisms of bioactive glass coatings during the HVSFS process, and employs for this purpose a well-known composition (whose bioactivity in bulk form has already been deeply characterised). This is namely, "45S5" bioglass, which has been the first bioactive glass ever developed and introduced on the market [1, 2, 36]. The microstructure of the HVSFS-deposited coatings was examined; their bioactivity was characterised by soaking in simulated body fluid (SBF) and compared to that of bulk 45S5 bioglass (obtained by casting), in order to check whether the spraying process could alter the known interaction processes between the 45S5 glass and SBF; what is more, the interaction of the coatings with osteoblast-like cells was characterised by in vitro cytotoxicity and cytocompatibility tests using MG63 cell line.

2 Experimental procedures

2.1 Preparation of powders and suspensions

The 45S5 bioglass, with chemical composition (in weight %) 45.0% SiO_2, 6.0% P_2O_5, 24.5% CaO, 24.5% Na_2O [1, 2, 36], was produced by mixing analytical-grade SiO_2, $Na_3PO_4{\cdot}12H_2O$, Na_2CO_3 and $CaCO_3$ (Carlo Erba Reagenti, Rodano, MI, Italy) in stoichiometric amounts. The mixture was melted at 1450°C for 1 h inside a Pt crucible, using an electrical furnace. A frit was then obtained by casting the molten glass into water, and was dry-milled in porcelain jars using Al_2O_3 balls. The resulting powders, sieved below 45 μm, were subsequently attrition milled in isopropanol for 3 h using 5 mm-diameter ZrO_2 balls and eventually dried for 24 h at 80°C.

Suspensions were produced by dispersing 20 wt% of attrition-milled powder in 80 wt% of a liquid phase consisting of 60 wt% water + 40 wt% isopropanol. A de-flocculating agent (Dolapix-65, 0.5 wt%) was also added to the suspension.

The attrition-milled glass powder was observed by SEM (XL30, FEI, Eindhoven, The Netherlands) and the size distribution in the suspension was measured by the laser diffraction technique (Mastersizer 2000, Malvern Instruments, Malvern, UK) after 5 min ultrasonic treatment. The rheological properties of the suspension was determined by rotating mode on a Physica MC200 rheometer device (Anton Paar GmbH, Graz, Austria): 100 ml of suspension

were tested in an aluminium beaker with a 45 mm-diameter cylindrical rotating measurement device, in the 0.1–500 s^{-1} shear rate range, at a constant temperature of 20°C.

For comparative purposes, one bulk bioglass sample was obtained by casting the molten raw material mixture in a graphite crucible, annealing at 550°C for 1 h and cooling in the oven.

2.2 Coating deposition

The HVSFS system has already been fully described in [35, 37]. The suspension, mechanically stirred along the whole process duration, was axially injected inside the combustion chamber of a TopGun-G high velocity oxygen-fuel (HVOF) torch (GTV GmbH, Luchenback, Germany) through a cylindrical nozzle, using a specially-designed feeding system. The torch was equipped with a 135 mm-long expansion nozzle featuring a conical combustion chamber.

The substrates were titanium grade 2 plates (50 × 50 mm^2), cleaned with acetone and then grit blasted with FEPA 120 fine corundum, using 5 bar blasting pressure. The surface roughness after the grit blasting process was $R_a = 1.49$ μm and $R_z = 9.99$ μm.

The HVSFS torch was mounted on a six axis robot and all of the coatings were deposited by performing 3 torch cycles, each consisting of a meander trajectory with 600 mm/s pass velocity and 2 mm inter-pass distance. Five different coatings were obtained by varying the suspension feed rate, the fuel (propane) and oxygen flow rates and the stand-off distance (Table 1). The system temperature was controlled by a pyrometer (Keller Pz10 AF1, Germany) focused on the front side of the samples. Before the deposition, the substrates were pre-heated to ~100°C by performing one preliminary torch cycle without injecting the suspension. During the deposition process, the substrates were simultaneously cooled by compressed air jets. The maximum deposition temperature was between 350 and 400°C, depending on the parameter set employed.

2.3 Structural and microstructural characterization

The phase composition of the bioglass coatings was assessed by X-ray diffraction (XRD: X'Pert PRO, PANAlytical, Almelo, The Netherlands), using Ni-filtered Cu–Kα radiation. Additional investigations were performed by micro-Raman spectrometry (Horiba Jobin–Yvon, Longjumeau, France) using a 632.81 nm-wavelength He–Ne laser as excitation source.

The microstructure of the samples was observed by SEM (XL30) on polished cross-sections (obtained by metallographic cutting, cold-mounted in resin, ground and polished with diamond slurry up to 0.5 μm) and fractured sections (obtained by breaking thin bars in liquid nitrogen).

The hardness and elastic modulus of the coatings were assessed by Berkovich nanoindentation (Nano-indentation tester, CSM Instrument, Peseux, Switzerland) on polished cross-sections (load: 100 mN; loading time: 10 s; loading/unloading rate: 80 mN/min), using the Oliver–Pharr method [38]. 15 indentations were performed in the middle of the coatings' cross-section.

2.4 Interaction with simulated body fluid (SBF)

In vitro immersion tests in a simulated body fluid (SBF) solution were performed on the bioglass coatings using samples of 10 mm × 10 mm, cut from the coated plates. In order to get a comparison, samples of identical size were also cut from the bulk bioglass.

These samples were immersed in SBF, prepared according to the detailed procedure described in [39]. The soaking tests were carried out in closed plastic containers, held at a constant temperature of 37°C in a controlled environment chamber (MPM Instruments S.r.l., Bernareggio, MI, Italy). Each container was filled with 20 ml of SBF solution and the samples were placed in vertical position (following the procedure described in [39]). Soaking times were 1, 3, 7, 14 and 28 days. After the extraction, the samples were rinsed in double-distilled water and dried at room temperature.

The chemical composition of the SBF solution was assessed after 1, 3, and 7 days of immersion by inductively

Table 1 Deposition parameters for the 45S5 bioglass coatings

Sample ID	O_2 flow rate (Sl/min)	Propane flow rate (Sl/min)	Stand-off distance (mm)	Suspension mass flow rate (g/s)	Torch speed (mm/s)	Pass distance (mm)
Bioglass #1	325	45	100	43	600	2
Bioglass #2	350	45	100	57	600	2
Bioglass #3	325	45	100	57	600	2
Bioglass #4	325	45	100	43	600	2
Bioglass #5	350	55	120	57	600	2

coupled plasma-optical emission spectrometry (ICP–OES: Varian 400, Agilent Technologies, Santa Clara, CA, USA).

The surfaces of the soaked samples were observed by Environmental Scanning Electron Microscopy (ESEM: Quanta 200, FEI) under low vacuum conditions (~0.67 mbar) and their polished cross-sections, cold-mounted in resin, were observed by SEM, as described previously. Qualitative chemical analyses were obtained by energy dispersive X-ray spectrometry (EDX: INCA 350, Oxford Instruments, Abingdon, UK). X-ray diffraction and micro-Raman spectroscopy were also performed on the coatings' surfaces (under the same experimental conditions listed above).

2.5 In vitro cell interaction

In vitro cytotoxicity and cytocompatibility tests were performed using a human osteosarcoma cell line MG63 (CRL 1427) model. Bioglass coatings were compared to commercially pure (c.p.) Ti (grade 2) samples, with acid-etched surfaces obtained according to the method described in Ref. [40]. This class of surfaces is considered a gold standard in some bone interface applications, such as dental implant surfaces [41]. Samples of 10 mm × 10 mm of bioglass coating #1 (as defined in Table 1) and samples of grade 2 titanium were obtained by mechanical cutting. Specimens were disinfected by soaking in 70% ethanol solution and then rinsed in sterile D.I. water.

Cytotoxicity tests were performed via immersion of five specimens in Eagle's minimal essential medium (EMEM) with 10% fetal bovine serum (FBS) and 1% penicillin/streptomycin/glutammine, maintaining a surface/medium ratio of 3 cm^2 ml^{-1}. Cultures were maintained in a 5% CO_2 humidified atmosphere at 37°C. After 2 or 7 days of incubation, medium extracts were put in contact with MG63 cells (density = 5×10^3 cells per well) in 96-well tissue culture plates (TCPs). Cells were cultured for 24 h and cell viability was investigated by MTT colorimetric assay (M5655, Sigma-Aldrich). MTT solution was added to each well and removed after 4 h of incubation at 37°C: formazan crystals were dissolved in dimethylsulfoxide (DMSO) and the absorbance measured at 570 nm with a spectrophotometer. Measurements for each specimen were triplicated.

In cytocompatibility tests seven specimens were seeded by using a cell density of 1×10^4 cells cm^{-2}. After 24 h, 3 and 7 days of incubation, cell viability was assessed using MTT colorimetric assay (5 specimens per each time point). To evaluate cell morphology at each time-point samples were prepared following a standard dehydration procedure [42] based on different ethanol concentrations and then observed with SEM.

Statistical analyses (Origin 6.0 software) were performed using a *t*-test (Student test), with significance level $P = 0.05$. Before each statistical test, normal distribution was verified by normal probability plots.

3 Results

3.1 Characterisation of the powder and suspension

The size distribution measured by laser diffraction on the suspension exhibits a slightly bimodal nature (Fig. 1a) and it is characterised by $d_{10} = 1.13$ µm, $d_{50} = 4.69$ µm, $d_{90} = 14.12$ µm. SEM micrographs (Fig. 1b), by contrast, show that the dry, attrition-milled powder contains many very fine (≤1 µm) particles, together with some coarse and angular ones, whose size ranges from ~5 µm to ~10 µm. The comparison between the SEM micrographs and the laser diffraction results suggests that the finer particles are largely agglomerated inside the suspension, in spite of the use of a 5 min-ultrasonic treatment before the laser diffraction measurement. This means the suspension has a certain tendency towards flocculation. Consistently, it shows a shear thinning behaviour (Fig. 2): its viscosity is higher (~0.2 Pa s) at low shear rates and decreases up to 0.01 Pa s at a shear rate of 100 s^{-1}, as large shear rates can disrupt the agglomerates.

3.2 Structural and microstructural characterisation of the coatings

The broad band appearing at $25° < 2\theta < 40°$ in the XRD patterns reveals that the coatings are entirely glassy; the only recognisable peaks, indeed, belong to the Ti substrate (Fig. 3a). Additionally, the micro-Raman spectra of the coatings are very similar to that of the bulk (cast and annealed) sample (Fig. 3b, c).

In all of the 45S5 bioglass coatings, the layers deposited during the three torch cycles (see Sect. 2.2) are easily recognisable, as an abundant fine porosity concentrates between them: these porous interlayer boundaries are marked by dash-dot lines on the polished cross-sections in Fig. 4a–e and by arrows on the fractured section view of Fig. 5a. It is also remarkable to note that the various layers have different thickness and porosity. More specifically, the first (bottom) layer is always the thinnest one and contains numerous small pores, whereas the third (topmost) layer becomes significantly (three times or more) thicker, with fewer and larger spherical pores. This difference becomes particularly obvious in coatings #2 and #3 (Fig. 4b, c), which were deposited using the highest suspension feed rate and low stand-off distance.

The large, rounded pores in the top layer resemble those which are typically found in conventional sintered glazes. This is due to the entrapment of air in the viscous material

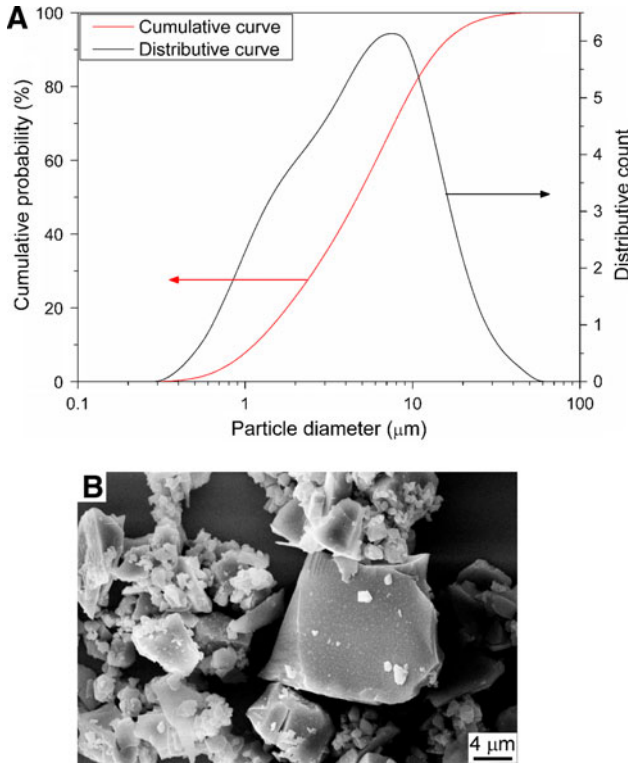

Fig. 1 Particle size distribution (**a**) and secondary electron SEM micrograph (**b**) of the attrition milled 45S5 bioglass powder

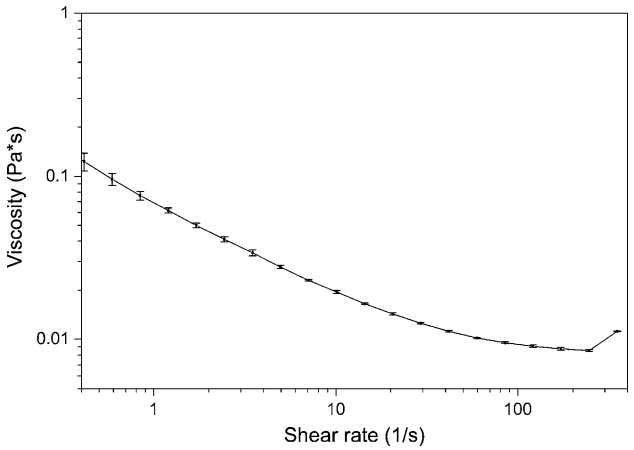

Fig. 2 Viscosity curve of the suspension obtained by dispersing 20 wt% of attrition-milled bioglass powder in 80 wt% of a water + isopropanol mixture

during the firing process [43]. The inter-layer porosity, by contrast, seems to be related to the presence of hollow rounded particles (see fractured sections on Fig. 5a, b): some of the pores are contributed by the intra-particle cavities, other are due to voids left between these incompletely-flattened particles. Numerous non-flattened hollow particles also seem to exist inside the first (bottom) layer of each coating (Figs. 4, 5). This actually accounts for its fine and homogeneously-distributed porosity.

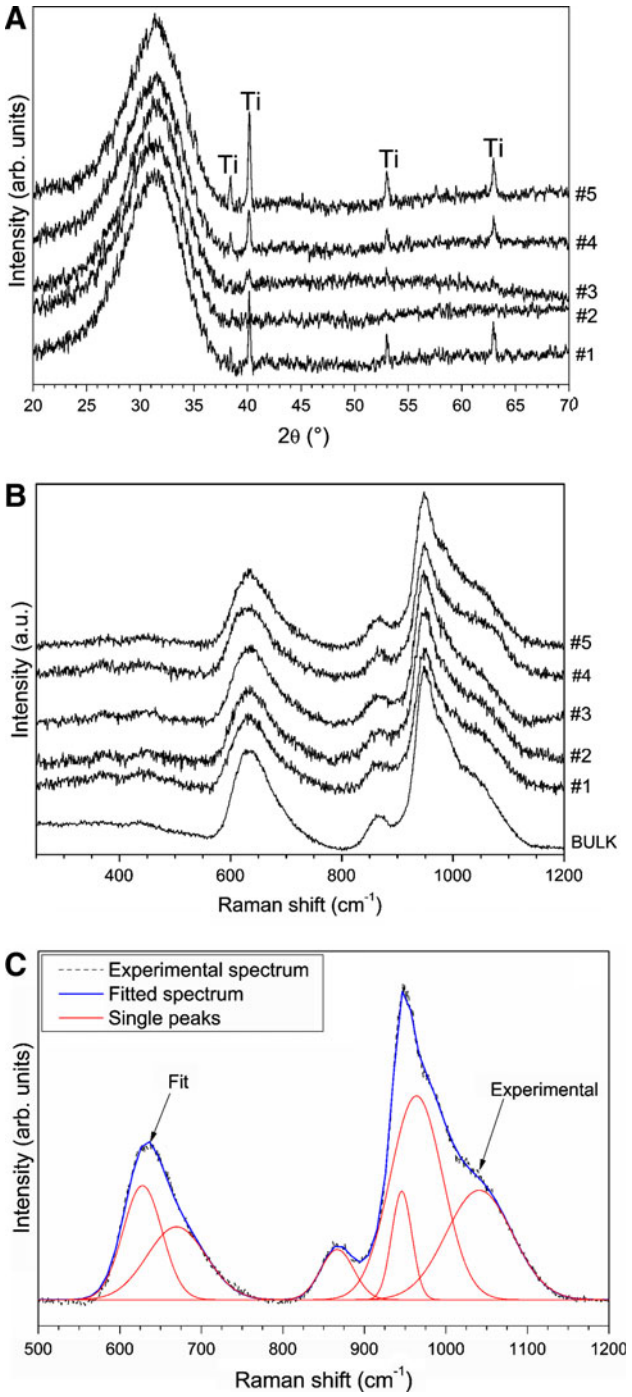

Fig. 3 XRD patterns (**a**) and micro-Raman spectra (**b**) acquired on the surface of the HVSFS-deposited bioglass coatings, and fitting of the Raman spectrum acquired on the bulk bioglass sample (**c**). Legend: Ti = titanium (JCPDS card n. 44-1294)

Also important to note, a thin film of titanium oxide exists on top of the substrate: it is recognisable as a thin dark layer in the cross-sectional micrographs of Fig. 4 and its presence is confirmed by the EDX line-scan analyses (Fig. 4f). The intensity of the Si–Kα peak also remains quite high while scanning through this thin layer (Fig. 4f,

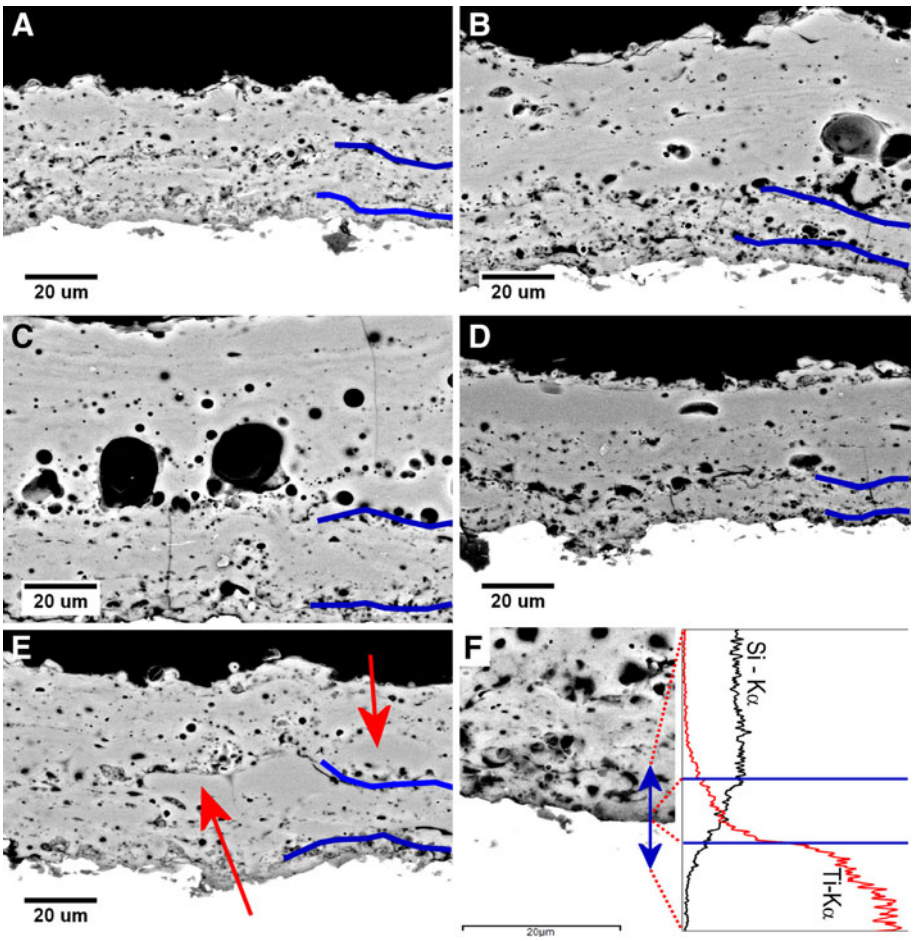

Fig. 4 Cross-sectional SEM micrographs (backscattered electrons) of the Bioglass-1 (**a**), 2 (**b**), 3 (**c**), 4 (**d**), 5 (**e**) coatings (*dash-dot lines* mark the boundaries between the three coating layers) and EDX line-scan analysis along the coating-substrate interface of Bioglass-4 sample (**f**)

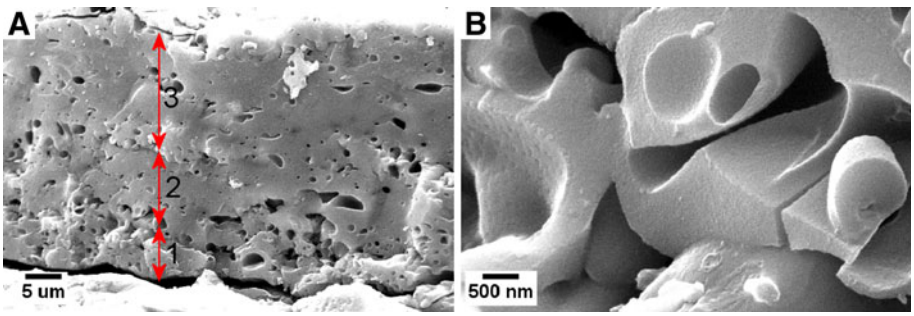

Fig. 5 Overview (**a**) and detail (**b**) of the fractured surface (secondary electron-SEM micrographs) of the Bioglass-2 coating. The *arrows* in panel (**a**) mark the three coating layers

see the region delimited by dashed lines); however, due to the quite poor lateral resolution of the EDX technique (the EDX signal generation region is $\geq$1 μm large), it is not possible to clarify whether some Si is actually present inside the Ti oxide layer.

The coatings #2 and #3, where the largest variations in layer thickness and morphology occur, are also the thickest and the hardest ones (Table 2). They also possess the largest average elastic modulus values; however, the differences between the elastic moduli of the present coatings are definitely small.

Table 2 Thickness and hardness of the HVSFS-deposited bioglass coatings

Sample ID	Thickness (μm)	Nanohardness (GPa)	Elastic modulus (GPa)
Bioglass #1	41 ± 3	2.9 ± 1.3	40 ± 12
Bioglass #2	71 ± 4	5.0 ± 0.8	53 ± 6
Bioglass #3	83 ± 15	4.8 ± 0.5	57 ± 8
Bioglass #4	47 ± 13	3.2 ± 1.4	43 ± 7
Bioglass #5	55 ± 6	3.4 ± 0.9	50 ± 5

3.3 Simulated body fluid (SBF) test

After soaking in SBF for 1 week, the bulk glass, and all of the HVSFS-deposited coatings, are uniformly covered by a film of precipitation products (Fig. 6). This film can already be identified after 1 day of soaking (Fig. 7a), and, on the HVSFS-deposited coatings, it always exhibits a "dome-like" morphology (Fig. 7a, b), which is presumably caused by its growth on top of a rough surface, i.e. the as-sprayed coating surface (Fig. 7c). The roughness of the precipitated film tends to decrease as the soaking time increases (Fig. 7a, b). Less "dome-like" features appear on the film developed on the bulk sample (Fig. 7d), on account of the lower roughness of the original surface of the cast and annealed glass.

None of the precipitated films is completely homogeneous, as some "clusters" appear (Fig. 6a, arrows) on their surfaces: they seem to be more numerous on the bulk glass samples than on the coatings (Fig. 6b–f). The films also appear microcracked (Fig. 6), because of the shrinkage occurring when they are dried after extraction from the SBF solution. Larger microcracks are found on samples soaked for longer times.

High-magnification views, inside these microcracks, reveal the film actually consists of two overlapping layers (Fig. 8a), which can be more clearly seen in cross-sectional SEM micrographs of both the coatings and the bulk sample (Fig. 8b, c). In both cases, the top layer (marked as "1st layer" in Fig. 8a–c) is much thinner; it appears brighter in backscattered electron imaging mode and contains large amounts of Ca and P (Fig. 8d, spectrum 1). The bottom layer (marked as "2nd layer" in Fig. 8a–c), by contrast, was found to be thicker and to consist almost entirely of Si and O ions (Fig. 8d, spectrum 2).

This precipitation layer is somewhat thicker on the HVSFS-deposited coatings than on the bulk glass sample (compare Fig. 8b, c) and becomes thicker with increasingly long immersion times; specifically, after 1 week of soaking, most of the original HVSFS-deposited bioactive glass coating has already been dissolved and replaced by the film (Fig. 8b): only a small layer of glass, whose chemical composition is slightly altered when compared to that of the original glass (Fig. 8d, spectra 3 and 4, respectively), is left. After 2 and 4 weeks, the entire HVSFS-deposited glass coating was replaced by the precipitated film.

When comparing the X-ray diffraction patterns, from all of the samples, to the reference one acquired on a pure hydroxyapatite powder (which is also perfectly consistent with the pattern listed in the JCPDS card 32-994), it can then be inferred, that hydroxyapatite was developed on the samples as a consequence of the precipitation phenomena occurred in SBF (Fig. 9a). The formation of hydroxyapatite starts after 1 day of soaking (Fig. 9b), consistently with the appearance of a precipitated film (Fig. 7a). The diffraction peaks of hydroxyapatite found in the soaked samples, however, are weaker and broader than the reference ones. The XRD patterns also indicate that the films formed on the bulk glass and on the coatings have analogous phase composition. Obviously, in the coated samples, the peaks of the titanium substrate (marked as Ti in Fig. 9a) also emerge, consistently with the patterns of the as-deposited coatings (Fig. 3a).

Consistent with these observations, the micro-Raman spectra acquired on the top surface of the samples (Fig. 9c, spectra 1 and 2), irrespective of the soaking time, also resemble closely the reference spectrum of the pure hydroxyapatite powder (Fig. 9c, spectrum 3), apart from a stronger peak at about 1075 cm^{-1}. The Raman spectrum acquired on the Si-rich layer (Fig. 9c, spectrum 4), by contrast, features a very broad band between 400 and 500 cm^{-1}, which resembles that of amorphous and/or hydrated silica [44–48].

ICP–OES analyses clearly reveal, after 1 day of soaking the amounts of PO_4^{3-}, Si and Ca in the test solution significantly increased (Table 3). The amounts of PO_4^{3-} and Ca then decreased slightly and tended to stabilize, whereas, the amount of Si continued to increase. The concentrations of Na and Mg, by contrast, did not vary significantly. It can also be noted, the samples are not releasing measurable amounts of Ti ions; analogously, no Al or Zr was released. These ions might have been present in the coatings as a result of contamination from the alumina balls employed in dry ball-milling or from the zirconia balls employed in attrition-milling, respectively; however, consistent with the absence of any perceivable contamination in the coatings, these ions were also not found in the test solution.

3.4 In vitro cell interaction

Cytotoxicity tests on extracts in contact with Bioglass specimens were performed at two different extraction times (2 and 7 days): absorbance values of MTT tests are summarized in Fig. 10a, compared to the fresh and 2 and 7 days aged medium. Results among the two time points and fresh medium are comparable in terms of cell viability: moreover, no significant differences ($P > 0.05$) were noticed between extracts and aged media for each time point.

Morphology of MG63 cells, adhered onto bioglass surfaces, are shown in Fig. 11 and results of biochemical assays (MTT test) in Fig. 10b. After 24 h of incubation (Fig. 11a), cells spread homogenously all over the Bioglass surface, extending their filopodia towards the surface asperities. By increasing the incubation time (Fig. 11b, c), surfaces appear progressively covered by a cell layer. SEM observations are confirmed by the absorbance values

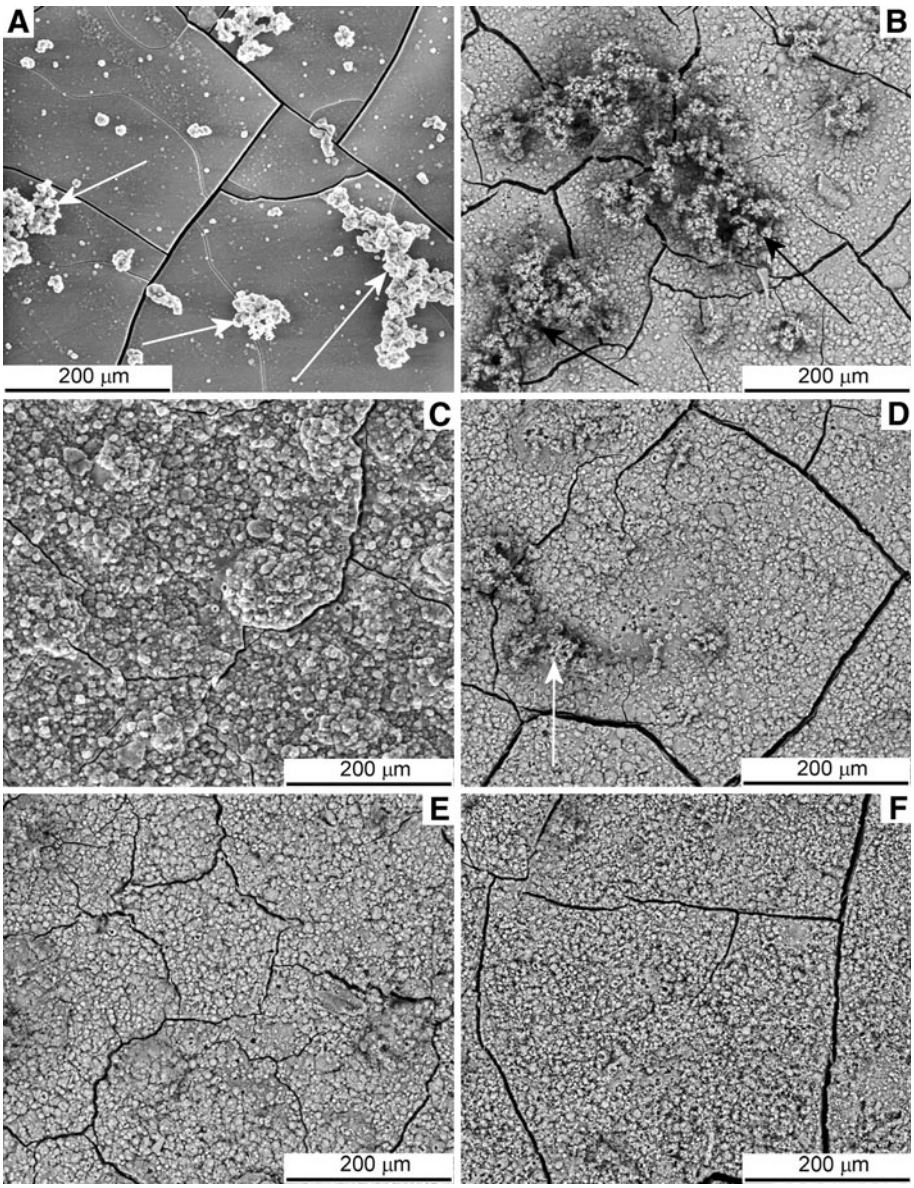

Fig. 6 Surface of the bulk bioglass (**a**) and of coatings #1 (**b**), #2 (**c**), #3 (**d**), #4 (**e**), #5 (**f**) after 1-week soaking in SBF (secondary electron ESEM micrographs)

related to the MTT assay (Fig. 10b): cell viability increased from the first to the 7th day after seeding and MG63 cell proliferation resulted similar onto both Bioglass and Ti surfaces.

4 Discussion

4.1 Coating deposition mechanisms

It is possible to propose a hypothesis on the coating formation mechanism, based on the results listed in Sects. 3.1 and 3.2, as well as on previous literature studies on suspension thermal spray coatings (and on HVSFS ones in particular). When a suspension stream is injected inside the gas jet of a thermal spray torch, various distinct phenomena occur sequentially: first, the stream is fragmented into small droplets, then the solvent is evaporated and individual particles or agglomerates are released [49–53]. The finer particles are often agglomerated [49–51], while some of the largest particles could be individually released.

As previously mentioned (in Sect. 3.1), agglomeration is most likely occurring for the present suspension; the shear-thinning behaviour (Fig. 2) suggests, the agglomerates are progressively disrupted as the shear rate increases. As the suspension injector has an internal diameter of 1.2 mm and it is about 20 mm long, an approximate estimation based on simple fluid dynamics equations suggests that a fully-developed laminar flow (Re $\sim$50 or less) can be established before reaching the injector exit. Due to the typical velocity profile of a laminar flow regime, the shear rate experienced by the suspension varies radially across the

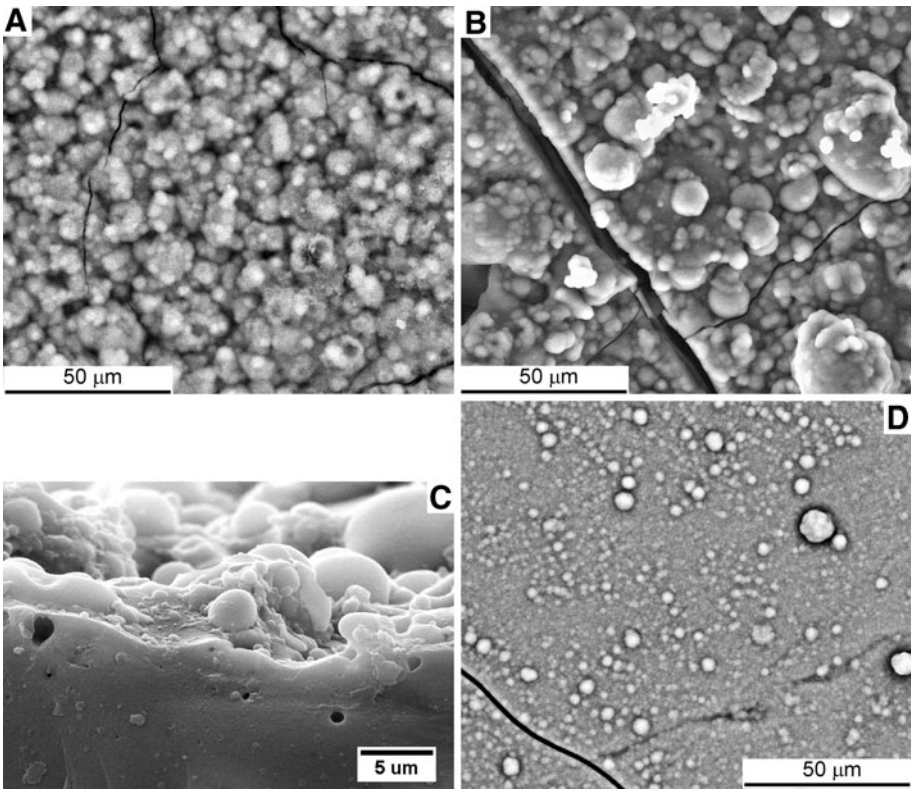

Fig. 7 Secondary electron SEM micrographs of the surface of the bioglass coating #1 after 1 day (**a**) and 1 week (**b**) soaking in SBF, of the fractured section of the same coating in as-deposited condition (viewed in the vicinity of the top surface) (**c**), and of the surface of the bulk bioglass sample after 1 week soaking (**d**)

injector, from a minimum (nominally equal to zero) along its axis to a maximum of $\sim 10^3$ s^{-1} close to the wall. Consequently, a wide agglomerate size distribution (presumably wider than that shown in Fig. 1a) enters the combustion chamber: it encompasses individual coarse particles, larger non-disrupted agglomerates, and finer agglomerates or individual fine particles, which result from the partial or total disruption of the original agglomerates because of the large shear rate close to the injector's wall. The coating is then produced by the impact of particles and agglomerates of very different size onto the substrate. The solvent evaporates quite quickly when it comes into contact with the combustion flame inside the combustion chamber and expansion nozzle (evaporation times are typically ~ 1 μs). The agglomerates (especially the smallest ones) may take a hollow morphology, as it occurs in spray-drying processes when the solvent evaporates very rapidly from a droplet [50, 53].

When depositing the first coating layer, the heated particles (or agglomerates) impinge directly onto a moderately pre-heated metallic substrate: the pre-heating temperature of about 100°C is well below the glass transition temperature of the 45S5 bioglass (Tg ≈ 540–550°C [54–56]). Consequently, the impinging glass is cooled down very rapidly: this might interfere with its spreading and flattening process by hindering the viscous flow of the heated material to some extent. Once the glass temperature approaches Tg, its viscosity starts to become bigger. This phenomenon probably affects all particles and agglomerates (independent of their retrospective size).

In fact, most of the large agglomerates, and coarse individual particles, cannot be properly heated during the short residence time inside the gas jet (few milliseconds). It is presumed, they are heated only along their outer boundary, whereas their core remains at low temperature (around or even below Tg) due to the low thermal conductivity. This is typical of glass. These results agree with previous research, which has shown that Al_2O_3 particles or agglomerates larger than 2.5 μm cannot be melted during the HVSFS process, using similar deposition parameters [37]. As these particles and agglomerates contact the substrate, the rapid cooling of their outer boundary by the metallic substrate, together with their low core temperature, prevents them from spreading and flattening; so that most likely they do not adhere. The result occurs with deposition efficiency being impaired.

By contrast, the smallest agglomerates or fine (sub-micrometric) individual particles can be heated up to high temperatures, however, they have such low inertia and heat capacity [57] that their velocity and temperature start decreasing before reaching the substrate. They can be deposited; although, their low kinetic energy (caused both by the decreasing impact velocity and by the low density of the glass, about 2.4 g/cm^3 [58]) and their low impact temperature, coupled with the additional cooling effect by the substrate, can cause them to freeze quite rapidly (below

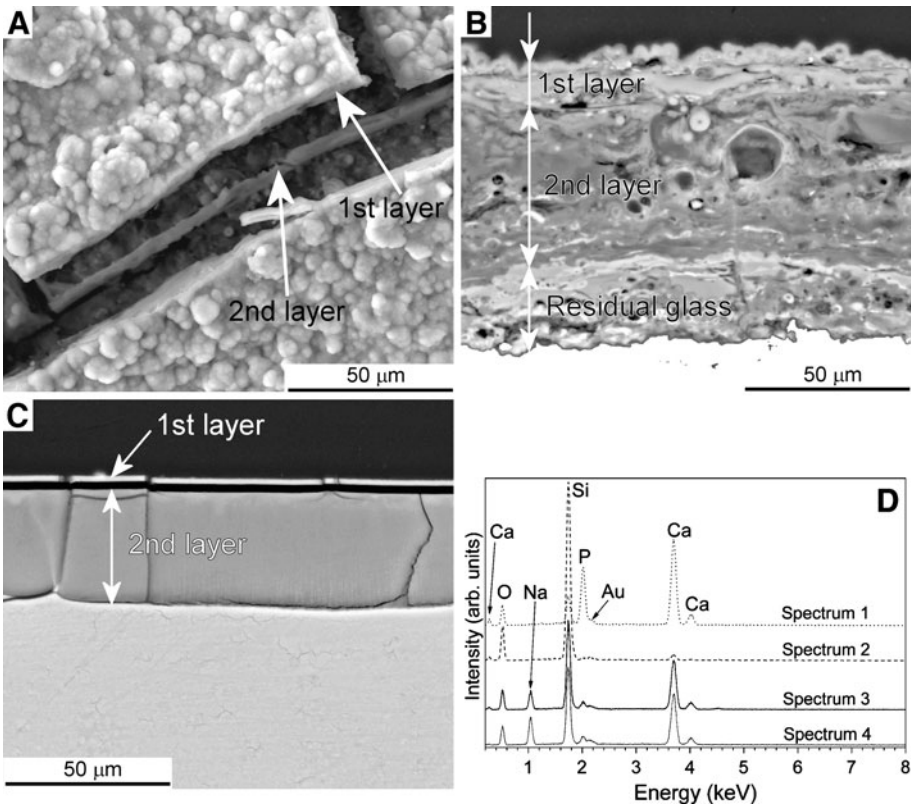

Fig. 8 SEM micrographs of the surface of the Bioglass #1 coating (**a** secondary electrons), of the cross-section of the Bioglass #2 coating (**b** backscattered electrons) and of the bulk bioglass (**c** backscattered electrons) after 1 week soaking in SBF. EDX analyses (**d**) of the 1st and 2nd layers in panels **a**, **b**, **c** (spectrum 1 and 2, respectively), of the residual glass in panel **b** (spectrum 3) and of the original glass (spectrum 4)

Tg) before they are able to spread significantly. This explains why the first layer contains fine non-flattened droplets (many of which retain their original hollow morphology) (Figs. 4, 5).

Only some particles or agglomerates, which have a size of few microns, are most likely to impinge on the substrate with adequate velocity and temperature in order to spread properly. Nonetheless, their flattening is somewhat restrained by the heat loss towards the substrate.

These considerations explain both the low thickness of the bottom layer (poor deposition efficiency because of the loss of the large particles) and its porosity (many non-flattened particles exist).

It is important to note, that during some of the preliminary experiments, pre-heating to $\sim 100°C$ was found to be of crucial importance: if the substrate was not pre-heated, or if it was allowed to cool again before spraying, it was impossible to deposit a homogeneous coating, regardless of the process parameters. If the substrate is not pre-heated, the freezing phenomena described above would most likely worsen. A warm substrate extracts heat from the impinging droplets at a slightly lower rate than a cold one. Additionally, the pre-heating process also enables the formation of a very thin Ti oxide layer on top of the substrate, which avoided the direct contact between the glass droplets and a purely metallic substrate. The formation of a Ti oxide layer during the deposition process is testified by the experimental observations shown in Fig. 4f and described in Sect. 3.2. Nonetheless, it is possible that the layer in Fig. 4f is somewhat thicker than the one formed during pre-heating, because this layer probably grew further while spraying the glass coating, as the system temperature increased continuously (up to 350–400°C, as indicated in Sect. 2).

More generally, another major effect produced when a substrate is pre-heated before spraying is the removal of adsorbates and condensates from its surface: adsorbates and condensates (e.g. humidity adsorbed on the substrate surface) have been shown to interfere with the spreading of thermally-sprayed droplets [59, 60]. In previous research on HVSFS-deposited Al_2O_3, however, high-quality coatings (dense and very hard) were deposited without any pre-heating [37, 61]. If the presence of adsorbates and condensates on the non pre-heated substrate were the most important reason for the poor efficiency during the deposition of the first glass layer, then it should have similarly affected the previous depositions of alumina coatings as well. This suggests, the most important role of pre-heating for the HVSFS-deposition of the bioglass coatings is the mitigation of the rapid cooling of glass droplets. Molten Al_2O_3 droplets are not affected by this rapid cooling as much as glass droplets. This is because the larger Reynolds

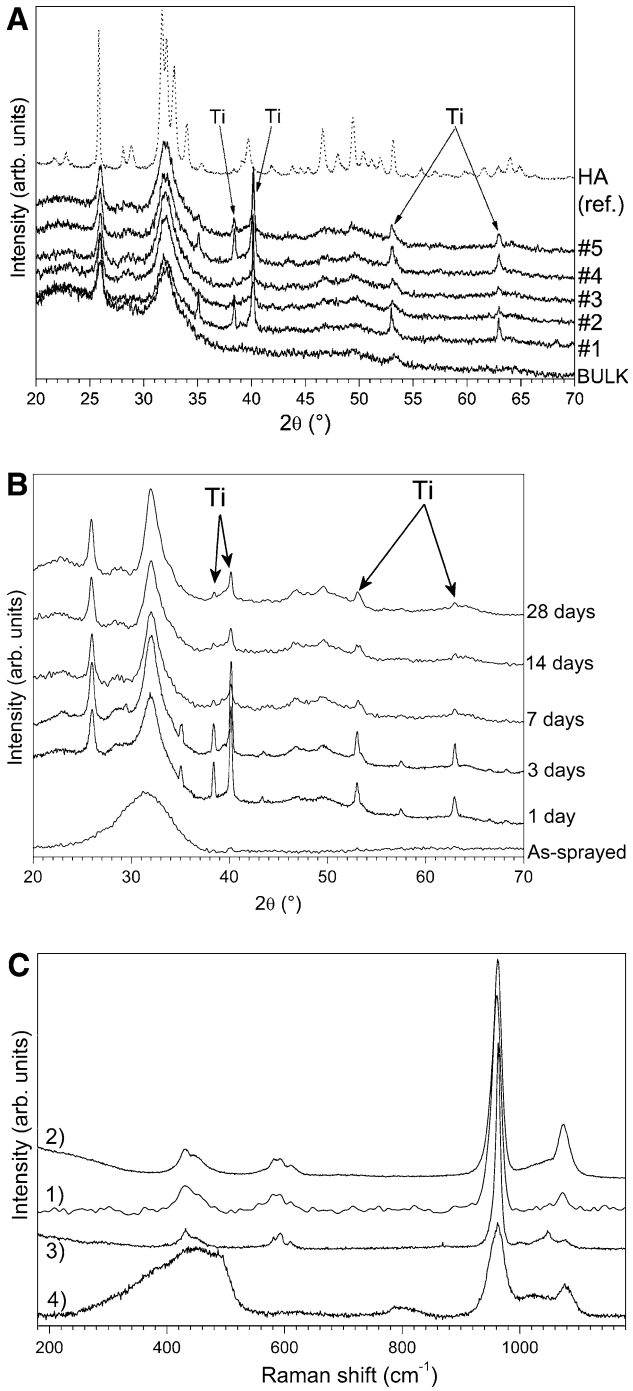

Fig. 9 XRD patterns of all samples after 1-week soaking in SBF, compared to that of a pure hydroxyapatite powder (**a**), and patterns of coating #3 after various soaking times (**b**); Raman spectra (**c**) acquired on the top surface of coating #1 after 1 day (spectrum 1) and 1 week (spectrum 2) of soaking in SBF, compared to the spectrum of pure hydroxyapatite powder (spectrum 3) and to the spectrum obtained by gently scraping the surface of a soaked sample (spectrum 4). Legend: Ti = titanium (JCPDS card n. 44-1294)

Table 3 Element and ion concentrations (in ppm) measured by inductively coupled plasma–optical emission spectrometry (ICP–OES) in the SBF solution before soaking tests and after soaking for 1, 3, 7 days

Soaking time	Ca	Na	Mg	Al	Ti	Zr	Si	PO_4^{3-}
No soaking	104.6	3875	46.5	0	0	0	3.8	1.6
1 day	114.7	3870	45.6	0	0	0	18.8	177.6
3 days	88.3	3904	44.1	0	0	0	36.5	67.4
7 days	92.1	3917	44.9	0	0	0	43.7	49.7

number of the former (alumina has indeed higher density and lower melt viscosity [58] than glass) favours more rapid flattening [60].

As shown in [62], the shock diamonds which develop inside the supersonic gas jet upon expansion to the atmosphere can affect the flight trajectory of particles and agglomerates. More specifically, some of the small glass particles and agglomerates could be ejected away from the axis of the gas jet into its fringes. Particles and agglomerates caught in the jet fringes are colder and slower than those residing in the middle of the jet. This is due to the gas temperature and velocity being lower. Consequently, these particles reach the target later than those in the jet core, and they cannot flatten extensively at impact: therefore, they are deposited on top of each coating layer and produce the interlayer porosity highlighted in Figs. 4, 5.

The subsequent coating layers are not deposited onto the metallic substrate, rather, onto an increasingly thick pre-existing glass coating. This latter is warmer and less thermally conductive than the substrate. When the glass droplets impinge onto such warm glass layer, they are then cooled at a much lower rate than on the substrate; as a result, they remain above Tg long enough to spread and adhere to the underlying material [58, 63]. Furthermore, the heat coming from the gas jet and from the droplets themselves could be sufficient for re-heating the surrounding glass above Tg. Larger agglomerates can therefore stick to the surrounding material and be embedded in the coating, even when they are not completely melted (see Fig. 4e, arrows), improving the deposition efficiency. The small hollow particles have time enough to flow and flatten, so that the overall porosity decreases. In particular, during the third cycle, the system temperature becomes so large that the glass particles remain above Tg during their whole spreading process: viscous flow sintering can therefore occur between adjacent lamellae [63].

All of these phenomena become particularly remarkable in coatings #2 and #3, which were sprayed with low stand-off distance and high suspension feed rate. During the first

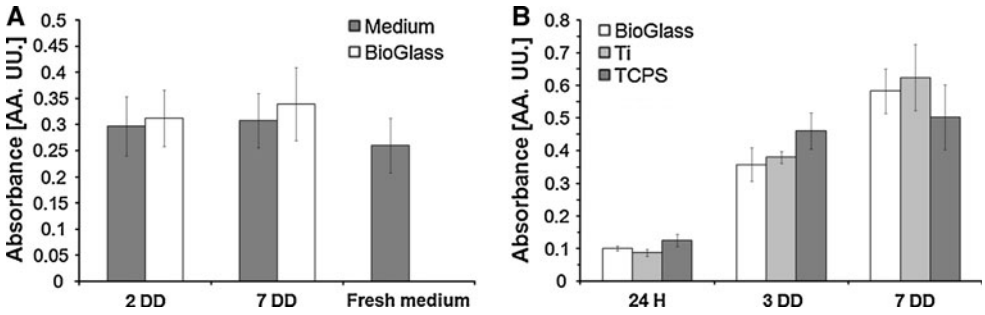

Fig. 10 In vitro viability MTT assays on MG63 cells: **a** cytotoxicity tests on fresh medium, aged medium, and Bioglass extract after 2 and 7 days; **b** Direct cytocompatibility tests on Bioglass, Ti, and TCPS versus culture time

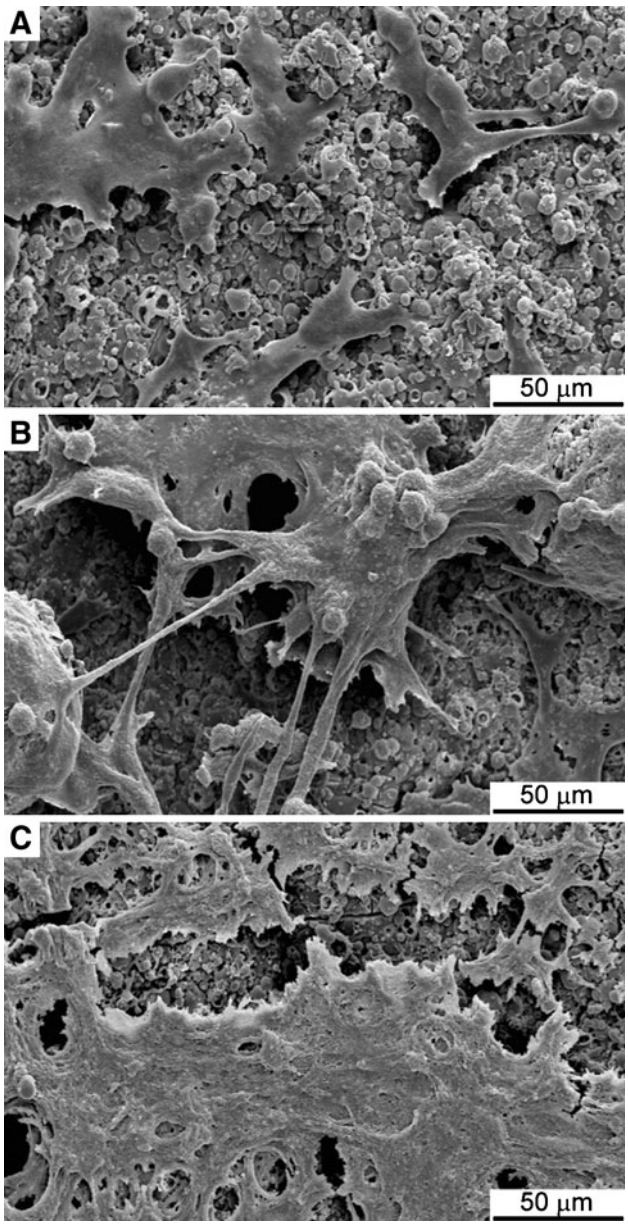

Fig. 11 SEM micrographs of MG63 cells on Bioglass coatings: **a** 1 day, **b** 3 days, and **c** 7 days

cycle, only a small fraction of the sprayed material adheres to the substrate, due to the above-mentioned problems. During the third one, instead, most of it is deposited, and the heat flow delivered by such large amount of impinging glass droplets is so huge that the entire topmost layer remains at $T > Tg$ for a sufficiently long time for large-scale viscous flow to occur. The fine pores are therefore able to coalesce into larger gas bubbles (Fig. 4b, c) [63]. These bubbles remained inside the coatings: while they had time enough to coalesce before the layer cooled below Tg, they did not have enough time to migrate. In fact, these samples were held vertically during the spraying process, which means the gas bubbles would tend to move parallel to the substrate (rather than toward the top surface).

The characteristics of the third layer, therefore, become quite similar to those of a bulk glass (sintered or annealed), and are evident in the results of the nanoindentation tests. The indentation marks were located in the middle of the coating thickness (as stated in Sect. 2); therefore, in coatings #2 and #3, most of them fall inside the third layer, which is at least twice as thick as the underlying ones, and reflect its properties. Accordingly, the hardness values measured on those coating (Table 2) resemble that of bulk 45S5 bioglass [2].

In coating #3, large tensile stresses were probably developed because of the extremely large amount of material deposited during the third pass, leading to the formation of some transverse cracks (Fig. 4c).

The process parameters therefore have remarkable effect on the coating properties (thickness, microstructure, porosity, etc.). Interlamellar sintering is a desirable phenomenon in order to improve the mechanical strength of the material and to remove the interlayer porosity: based on the previous discussion on the effect of shock diamond in expelling particles into the cold jet fringes, indeed, it may be concluded that interlayer porosity should be regarded as an intrinsic feature of the HVSFS process, particularly when depositing low density materials, such as glasses, which are particularly sensitive to those effects; therefore, the elimination of interlayer porosity must primarily rely on sintering phenomena occurring during the deposition of

subsequent layers. On the other hand, excessive overheating of the sprayed material, which results in the formation of excessively large rounded gas bubbles in the topmost layers and in transverse cracking because of tensile stresses, is an undesirable phenomenon which can compromise the mechanical strength of the coating. While further work shall also be addressed to the measurement of mechanical properties (such as adhesion/cohesion measured by tensile adhesion testing), elimination of such porosity should be a goal of further process parameter optimisation. Analogously, control over coating thickness is also to be acquired. For instance, most thermally-sprayed hydroxyapatite coatings for orthopaedic applications are generally required to be <100 μm thick [64, 65]: if this criterion should apply to bioglass coatings as well (the effect of the thickness of bioactive glass layers on the stability and bone bonding of coated implants should be ascertained by future work including in vivo tests), coatings #1, #4, #5 can be deemed suitable, whereas coatings #2 and #3 are excessively thick and might pose problems of excessive residual stress and brittleness.

4.2 Glass structure and interactions with the simulated body fluid (SBF)

XRD patterns and Raman spectroscopy (Fig. 3a, b) indicate that the glass underwent no structural alteration during the deposition process, as expected based on the previous experiences summarised in the Introduction. The glass did not crystallise (Fig. 3a), although the material in the third layer remained at T > Tg for some time, as discussed in Sect. 4.1: either its temperature remained below the threshold for the onset of crystallisation [55], or the time spent at high temperature was not long enough for crystallisation to take place. Additionally, the 3-D glass network of the coatings is not appreciably different from that of the bulk material (Fig. 3b) and all of the Raman spectra are perfectly consistent with those reported in Ref. [56]. By fitting the present spectra using Gaussian functions (as shown in Fig. 3c for the bulk sample), it was found that the main peaks are located at 628, 670, 867, 946, 964 and 1041 cm^{-1}. The peak at 946 cm^{-1}, in particular, is related to the presence of chain and ring silicate structures [56], and reflects the interruption of the three-dimensional silica network because of the presence of modifiers, such as Na, in the glass composition: the weakened network is an essential structural feature of bioactive glasses, as it enables their controlled dissolution in body fluids [1, 2, 24, 66]. The peak at 964 cm^{-1}, instead, is contributed by the phosphate units present within the glass [56].

On account of their substantial structural analogy, the bulk bioglass and the HVSFS-deposited coatings exhibit similar interactions with SBF. In all cases, the controlled dissolution of the glass network induces the precipitation of a 2-layer film on top of the sample surface: based on ESEM micrographs and EDX analyses (Figs. 6, 7, 8) as well as on XRD patterns and Raman spectra (Fig. 9), it can be inferred that the bottom layer consists of amorphous (and possibly hydrated) silica, whereas the top layer would seem to consist of hydroxyapatite. The broad halo existing in the XRD patterns between 20° and 25° is related to the silica-rich layer [67], whereas the remaining diffraction peaks, as stated in Sect. 3.3, are related to the formation of hydroxyapatite. The reaction seems to be very fast, as 1 day of soaking is enough to produce a recognisable layer of hydroxyapatite on the samples' surface (Figs. 7a, 9b, c).

The remarkable broadening of the diffraction peaks of hydroxyapatite in the 2θ range between 31° and 33° (Fig. 9a, b) could be due to the existence of structural defects or alterations in the present layer. It also reflects the micro-crystalline nature of the layer [67]. A discrepancy also appears in the Raman spectra (Fig. 9c), as a quite strong peak at 1075 cm^{-1} arises out of the precipitated layer, whereas, pure hydroxyapatite exhibits multiple, weaker peaks, in the 1020–1100 cm^{-1} range (related to the *v3* vibration mode of the PO_4^{3-} structural units) [68, 69]. Based on previous literature studies, this difference probably witnesses to the formation of carbonated hydroxyapatite, a common phenomenon for bioactive glasses immersed in simulated body fluid solutions for sufficiently long times [24, 70–72]. The presence of carbonate groups within the structure of such layer can obviously account for the above-mentioned structural alterations causing the broadening of XRD peaks.

These observations confirm that the interaction mechanisms of the 45S5 bioglass with SBF follow the well-known sequence, described in several literature papers [1, 2, 24, 29, 72]. During the first few hours of immersion, alkali and alkali-earth ions are rapidly exchanged with H^+ (or H_3O^+) from the solution and Si–O–Si bonds are progressively broken, with loss of soluble silica in the form of $Si(OH)_4$: these events are clearly witnessed by the remarkable increase of the Ca and Si concentrations in the SBF solution after just 1 day of soaking (Sect. 3.3 and Table 3). Part of the dissolved silica is then deposited again onto the sample surface and polymerises into a SiO_2-rich layer (silica gel). A $CaO–P_2O_5$-rich layer then develops on top of the silica gel, which is contributed by the Ca^{2+} and $(PO_4)^{3-}$ groups coming from the glass through the silica layer, and by those precipitating from the solution. This causes the concentration of Ca and PO_4^{3-} in the solution to stabilise, whereas some release of soluble silica still goes on at this stage. This layer, which also incorporates OH^-, $(CO_3)^{2-}$ and F^- ions from the solution, soon crystallises into carbonated hydroxyapatite. Its formation follows a typical nucleation and growth mechanism, which is

testified by its "dome-like" morphology: isolated nuclei, developed at some specific locations on the surface of the silica gel, grow and expand into domes, which come into contact with each other in less than 1 day, developing a continuous film. Once the domes are in contact, further growth causes better overlapping and more uniform coverage of the surface, making the film progressively smoother.

The formation of a double layer is known to be typical of the interaction of bioactive glasses with aqueous media [73]. The present study, therefore, leads to the fundamental conclusion that this mechanism (which was obviously expected for the bulk annealed glass), also holds for the HVSFS-deposited coatings. This is of particular importance, due to the fact, this particular interaction is the basis for the subsequent adhesion and proliferation of bone tissues onto the surface of the glass. The carbonated hydroxyapatite layer is, indeed, chemically and structurally similar to bone tissue itself [1, 2, 24, 29]. Furthermore, the Si ions released into the body fluids might further stimulate the development and bonding of bone tissues to the surface of the bioactive glass [1, 25, 26]. The effectiveness of such mechanism is proved by the stronger adhesion of bone tissues to bulk bioglass than to bulk hydroxyapatite. This fact is mentioned in the references cited above.

The reactivity of the bulk glass and that of the HVSFS-deposited coatings with the SBF only differ in the thickness and morphology of the two layers. The thickness of the SBF-affected region is indeed larger in the HVSFS-deposited coatings: because of their porosity, their actual contact area with the SBF is wider than that of the bulk sample. Moreover, the layer developed on the HVSFS-deposited coatings is slightly rougher.

4.3 Cytocompatibility and cytotoxicity

Several formulations of bioactive glasses have been proposed as bone graft and bone contact materials, after the first formulations proposed by Hench in the late 1960s [1, 2, 36]. They are similar to other bone grafts, such as hydroxypatite and tricalcium phosphate, which are highly biocompatible and show the ability to bond directly to bone [74], possessing osteoconductive and osteostimulative properties [75]. Cytotoxicity and cell interaction tests were previously performed in order to investigate Bioglasses as orthopedic materials, showing the ability of this class of materials in supporting the growth of human bone-forming cells [74] and to regulate functional activities [76]. These materials were shown to promote bone healing in several in vivo models [75].

Here, through a human osteoblast-like cell line (MG63), the 45S5 bioglass formulation is shown to maintain its biofunctionality when sprayed via HVSFS onto titanium substrate. MG63 cell line is a validated model to test the biocompatibility and was used in several previous works on such a substrate [74–76]. More specifically, extract analysis based on MTT viability assay shows that no toxic products are released by Bioglass coatings obtained via HVSFS. Furthermore, cell proliferation tests showed the ability of HVSFS coatings to support an increasing viability, with no statistical differences when compared to an acid-etched titanium surface that is commonly used in bone-contact dental applications. SEM micrographs represent a useful tool for the assessment of cell behaviour, particularly for attachment, adhesion, proliferation and ECM matrix production [74]. From the present SEM observations, no adverse changes in cell morphology onto HVSFS Bioglass surfaces were observed: for culture time up to 7 days, HVSFS Bioglass surfaces support the growth and cell division, with morphological characteristics similar to those observed on other thermally-sprayed bioactive coatings in previously published works [77–80].

5 Conclusions

Bioactive glass powders based on the well-known "45S5" bioglass composition were prepared, dispersed in a water + isopropanol suspension and thermally-sprayed onto pre-heated Ti plates by the HVSFS technique.

The resulting coatings exhibit a microstructural gradient, as the deposition mechanisms vary during the deposition process itself. When the first coating layer is sprayed onto the moderately pre-heated Ti substrate, the very fast cooling of the impinging glass droplets hinders their adhesion and flattening, so that a thin layer containing abundant fine porosity is obtained. The subsequent layers are deposited onto an increasingly warm glass surface, which does not cool the impinging droplets equally fast; denser and thicker layers are therefore obtained and large-scale viscous flow sintering of the entire layer can eventually occur if the sprayed glass remains long enough at $T > Tg$.

The sprayed coatings are entirely glassy and the glass network structure (characterised by Raman spectroscopy) is analogous to that of bulk annealed 45S5 bioglass. This means, the glass undergoes no structural alteration during the spraying process. Consequently, the interaction mechanisms between the coatings and the simulated body fluid (SBF) are also analogous to those of the bulk bioglass, and involve controlled dissolution of the glass, polymerisation of an amorphous silica layer onto the glass surface itself and growth of a carbonated hydroxyapatite layer on top of the silica layer. This interaction is particularly fast, as only 1 day soaking in SBF is needed in order to develop a continuous hydroxyapatite layer onto the surface of the samples.

In vitro tests indicate that HVSFS bioglass surfaces are a suitable substrate for human osteoblast-like cell adhesion and proliferation, maintaining the biocompatibility characteristic of bulk bioglass. In particular, biochemical assays and morphological observation confirm that this material appears suitable for bone-contact applications.

Consequently, all of these results suggest, there is a possibility to use HVSFS-deposited 45S5 bioactive glass coatings in order to promote osseointegration of metallic prosthesis, as an alternative to thermally-sprayed hydroxyapatite. Compared to the latter, bioglass poses no troubles related to decomposition and phase alteration. The reactivity of the HVSFS-deposited bioglass coatings seems to be particularly fast, as most of the original coating was replaced by the products of the interaction with the SBF in only one week: these coatings might therefore be especially useful in those applications where short osseointegration times and progressive resorption of the bioactive layer are required.

Further work should aim to elucidate the most promising application fields for these coatings and to optimize their microstructure, by improving the deposition efficiency during the first torch cycle, and by reducing the overall porosity. For instance, a possibility would be to deposit a ceramic bond coat (e.g. TiO_2), similarly to previous researches on plasma-sprayed hydroxyapatite coatings [17, 81], and to pre-heat the system to larger temperatures before spraying the bioglass.

Acknowledgements L. Altomare and L. De Nardo thank Dr. Monica Moscatelli and Prof. Silvia Farè for technical support in cell culture tests and acknowledge MIUR for FIRB grant "SAST". L. De Nardo thanks Politecnico di Milano (Grant: 5 per Mille Junior) and the Italian Institute of Technology (IIT) for economic support.

References

1. Cao W, Hench LL. Bioactive materials. Ceram Int. 1996;22:493–507.
2. Hench LL. Bioceramics. J Am Ceram Soc. 1998;81:1705–28.
3. Gross KA, Berndt CC. Biomedical application of apatites. In: Kohn MJ, Rakovan J, Hughes JM, editors. Phosphates: geochemical, geobiological, materials importance—reviews in mineralogy, geochemistry, vol. 48. Washington DC, USA: Mineralogical Society of America; 2002. p. 631–72.
4. Liu X, Chu PK, Ding C. Surface modification of titanium titanium alloys, and related materials for biomedical applications. Mater Sci Eng R. 2004;47:49–121.
5. Sun L, Berndt CC, Gross KA, Kucuk A. Material fundamentals and clinical performance of plasma-sprayed hydroxyapatite coatings: a review. J Biomed Mater Res. 2001;58:570–92.
6. García C, Ceré S, Durán A. Bioactive coatings deposited on titanium alloys. J Non-Cryst Solids. 2006;352:3488–95.
7. Kačiulis S, Mattogno G, Pandolfi L, Cavalli M, Gnappi G, Montenero A. XPS study of apatite-based coatings prepared by sol–gel technique. Appl Surf Sci. 1999;151:1–5.
8. Gyorgy E, Grigorescu S, Socol G, Mihailescu IN, Janackovic D, Dindune A, Kanepe Z, Palcevskis E, Zdrentu EL, Petrescu SM. Bioactive glass and hydroxyapatite thin films obtained by pulsed laser deposition. Appl Surf Sci. 2007;253:7981–6.
9. Yang Y, Kim K-H, Ong JL. A review on calcium phosphate coatings produced using a sputtering process—an alternative to plasma spraying. Biomaterials. 2005;26:327–37.
10. Trommer RM, Santos LA, Bergmann CP. Alternative technique for hydroxyapatite coatings. Surf Coat Technol. 2007;201:9587–93.
11. Paital SR, Dahotre NB. Calcium phosphate coatings for bio-implant applications: materials performance factors, and methodologies. Mater Sci Eng R. 2009;66:1–70.
12. de Groot K, Wolke JGC, Jansen JA. Calcium phosphate coatings for medical implants. Proc Inst Mech Eng H J Eng Med. 1998;212:137–47.
13. Herman H, Sampath S, McCune R. Thermal spraying: current status and future trends. Mater Res Soc Bull. 2000;25(7):17–25.
14. Sun L, Berndt CC, Khor KA, Cheang NH, Gross KA. Surface characteristics and dissolution behavior of plasma-sprayed hydroxyapatite coating. J Biomed Mater Res. 2002;62:228–36.
15. Dyshlovenko S, Pawlowski L, Roussel P, Murano D, Le Maguer A. Relationship between plasma spray operational parameters and microstructure of hydroxyapatite coatings and powder particles sprayed into water. Surf Coat Technol. 2006;200:3845–55.
16. Dyshlovenko S, Pawlowski L, Pateyron B, Smurov I, Harding JH. Modelling of plasma particle interactions and coating growth for plasma spraying of hydroxyapatite. Surf Coat Technol. 2006;200:3757–69.
17. Heimann RB. Thermal spraying of biomaterials. Surf Coat Technol. 2006;201:2012–9.
18. Pierlot C, Pawlowski L, Tomaszek R, Dyshlovenko S, Bigan M. Interdependence of different properties of hydroxyapatite coatings and powders plasma sprayed into water. Chemom Intell Lab Syst. 2007;86:153–8.
19. Dyshlovenko S, Pierlot C, Pawlowski L, Tomaszek R, Chagnon P. Experimental design of plasma spraying and laser treatment of hydroxyapatite coatings. Surf Coat Technol. 2006;201:2054–60.
20. Yang C-W, Lee T-M, Lui T-S, Chang E. Effect of post vacuum heating on the microstructural feature and bonding strength of plasma-sprayed hydroxyapatite coatings. Mater Sci Eng C. 2006;26:1395–400.
21. Lugscheider E, Knepper M, Nyland A. Characterization of thermal sprayed bioactive coatings. Colloids Surf B. 1996;6:1–7.
22. Gabbi C, Cacchioli A, Locardi B, Guadagnino E. Bioactive glass coating: physicochemical aspects and biological findings. Biomaterial. 1995;16:515–20.
23. Schrooten J, Helsen JA. Adhesion of bioactive glass coating to Ti6Al4V oral implant. Biomaterial. 2000;21:1461–9.
24. Lee TM, Chang E, Wang BC, Yang CY. Characteristics of plasma-sprayed bioactive glass coatings on Ti–6A1–4V alloy: an in vitro study. Surf Coat Technol. 1996;79:170–7.
25. Oliva A, Salerno A, Locardi B, Riccio V, Della Ragione F, Iardino P, Zappia V. Behaviour of human osteoblasts cultured on bioactive glass coatings. Biomaterial. 1998;19:1019–25.
26. Foppiano S, Marshall SJ, Marshall GW, Saiz E, Tomsia AP. Bioactive glass coatings affect the behavior of osteoblast-like cells. Acta Biomater. 2007;3:765–71.
27. Lopez-Estebana S, Saiz E, Fujino S, Oku T, Suganuma K, Tomsia AP. Bioactive glass coatings for orthopedic metallic implants. J Eur Ceram Soc. 2003;23:2921–30.
28. Bolelli G, Lusvarghi L, Manfredini T, Siligardi C. Influence of the manufacturing process on the crystallization behavior of a CZS glass system. J Non-Cryst Solids. 2005;351:2537–46.
29. Höland Wolfram. Biocompatible and bioactive glass-ceramics—state of the art and new directions. J Non-Cryst Solids. 1997;219:192–7.

30. Killinger A, Kuhn M, Gadow R. High-velocity suspension flame spraying (HVSFS), a new approach for spraying nanoparticles with hypersonic speed. Surf Coat Technol. 2006;201:1922–9.
31. Rauch J, Bolelli G, Killinger A, Gadow R, Cannillo V, Lusvarghi L. Advances in high velocity suspension flame spraying (HVSFS). Surf Coat Technol. 2009;203:2131–8.
32. Gadow R, Killinger A, Rauch J. New results in high velocity suspension flame spraying (HVSFS). Surf Coat Technol. 2008;202:4329–36.
33. Bolelli G, Rauch J, Cannillo V, Killinger A, Lusvarghi L, Gadow R. Investigation of high-velocity suspension flame sprayed (HVSFS) glass coatings. Mater Lett. 2008;62:2772–5.
34. Cannillo V, Pierli F, Sampath S, Siligardi C. Thermal and physical characterisation of apatite/wollastonite bioactive glass–ceramics. J Eur Ceram Soc. 2007;27:4575–88.
35. Bolelli G, Cannillo V, Gadow R, Killinger A, Lusvarghi L, Rauch J. Microstructural and in vitro characterisation of high-velocity suspension flame sprayed (HVSFS) bioactive glass coatings. J Eur Ceram Soc. 2009;29:2249–57.
36. Hench LL. Bioceramics: from concept to clinic. J Am Ceram Soc. 1991;74:1487–510.
37. Bolelli G, Cannillo V, Gadow R, Killinger A, Lusvarghi L, Rauch J, Romagnoli M. Effect of the suspension composition on the microstructural properties of high velocity suspension flame sprayed (HVSFS) Al_2O_3 coatings. Surf Coat Technol. 2010;204:1163–79.
38. Oliver WC, Pharr GM. An improved technique for determining hardness and elastic modulus using load and displacement sensing indentation experiments. J Mater Res. 1992;7:1564–83.
39. Kokubo T, Takadama H. How useful is SBF in predicting in vivo bone bioactivity? Biomaterial. 2006;27:2907–15.
40. Giordano C, Sandrini E, Busini V, Chiesa R, Fumagalli G, Giavaresi G, Fini M, Giardino R, Cigada A. A new chemical etching process to improve endosseous implant osseointegration: In vitro evaluation on human osteoblast-like cells. Int J Artif Organs. 2006;29:772–80.
41. De Nardo L, Raffaini G, Ganazzoli F, Chiesa R. Surface modification of biomaterials: methods, analysis and applications. In: Williams R, editor. Metal surface oxidation and surface interactions. Cambridge: Woodhead; 2011. p. 102–42.
42. De Nardo L, Moscatelli M, Silvi F, Tanzi MC, Yahia LH, Farè, S. Chemico-physical modifications induced by plasma and ozone sterilizations on shape memory polyurethane foams. J Mater Sci Mater Med. 2010;21:2067–78.
43. Bolelli G, Cannillo V, Lusvarghi L, Manfredini T, Siligardi C, Bartuli C, Loreto A, Valente T. Plasma-sprayed glass-ceramic coatings on ceramic tiles: microstructure, chemical resistance and mechanical properties. J Eur Ceram Soc. 2005;25:1835–53.
44. Gout R, Oelkers EH, Schoit J, Zwick A. The surface chemistry and structure of acid-leached albite: New insights on the dissolution mechanism of the alkali feldspars. Geochim Cosmochim Acta. 1997;61:3013–8.
45. Gao X, Wachs IE. Structural characteristics and reactivity properties of highly dispersed Al_2O_3/SiO_2 and $V_2O_5/Al_2O_3/SiO_2$ catalysts. J Catal. 2000;192:18–28.
46. Galeener FL, Mikkelsen JC Jr. Raman studies of the thermal oxide of silicon. Solid State Commun. 1981;37:719–23.
47. Xie S, Iglesia E, Bell AT. Effects of hydration and dehydration on the structure of silica-supported vanadia species. Langmuir. 2000;16:7162–7.
48. Murray CA, Gretyak TJ. Intrinsic surface phonons in amorphous silica. Phys Rev B Condens Matter Mater Phys. 1979;20:3368–87.
49. Delbos C, Fazilleau J, Rat V, Coudert JF, Fauchais P, Pateyron B. Phenomena involved in suspension plasma spraying. Part 2: zirconia particle treatment and coating formation. Plasma Chem Plasma Process. 2006;26:393–414.
50. Kaβner H, Vaβen R, Stöver D. Study on instant droplet and particle stages during suspension plasma spraying (SPS). Surf Coat Technol. 2008;202:4355–61.
51. Fauchais P, Rat V, Coudert J-F, Etchart-Salas R, Montavon G. Operating parameters for suspension and solution plasma-spray coatings. Surf Coat Technol. 2008;202:4309–17.
52. Oberste Berghaus J, Legoux J-G, Moreau C, Tarasi F, Chráska T. Mechanical and thermal transport properties of suspension thermal-sprayed alumina-zirconia composite coatings. J Therm Spray Technol. 2008;17:91–104.
53. Pawlowski L. Suspension and solution thermal spray coatings. Surf Coat Technol. 2009;203:2807–29.
54. Lefebvre L, Gremillard L, Chevalier J, Zenati R, Bernache-Assolant D. Sintering behaviour of 45S5 bioactive glass. Acta Biomater. 2008;4:1894–903.
55. Lefebvre L, Chevalier J, Gremillard L, Zenati R, Thollet G, Bernache-Assolant D, Govin A. Structural transformations of bioactive glass 45S5 with thermal treatments. Acta Mater. 2007;55:3305–13.
56. Lin C-C, Huang L-C, Shen P. $Na_2CaSi_2O_6$–P_2O_5 based bioactive glasses. Part 1: elasticity and structure. J Non-Cryst Solids. 2005;351:3195–203.
57. Dongmo E, Wenzelburger M, Gadow R. Analysis and optimization of the HVOF process by combined experimental and numerical approaches. Surf Coat Technol. 2008;202:4470–8.
58. Poirier T, Planche MP, Landemarre O, Coddet C. Particles spreading phenomena in the case of glass thermal spraying. J Therm Spray Technol. 2008;17:564–73.
59. Jiang X, Wan Y, Herman H, Sampath S. Role of condensates and adsorbates on substrate surface on fragmentation of impinging molten droplets during thermal spray. Thin Solid Films. 2001;385:132–41.
60. Chandra S, Fauchais P. Formation of solid splats during thermal spray deposition. J Therm Spray Technol. 2009;18:148–80.
61. Bolelli G, Rauch J, Cannillo V, Killinger A, Lusvarghi L, Gadow R. Microstructural and tribological investigation of high-velocity suspension Flame sprayed (HVSFS) Al_2O_3 coatings. J Therm Spray Technol. 2009;18:35–49.
62. Srivatsan VR, Dolatabadi A. Simulation of particle-shock interaction in a high velocity oxygen fuel process. J Therm Spray Technol. 2006;15:481–7.
63. Arcondéguy A, Grimaud A, Denoirjean A, Gasgnier G, Huguet C, Pateyron B, Montavon G. Flame-sprayed glaze coatings: effects of operating parameters and feedstock characteristics onto coating structures. J Therm Spray Technol. 2007;16:978–90.
64. Gross KA, Saber-Samandari S, Heemann KS. Evaluation of commercial implants with nanoindentation defines future development needs for hydroxyapatite coatings. J Biomed Mater Res B. 2010;93:1–8.
65. Cao N, Dong J, Wang Q, Ma Q, Xue C, Li M. An experimental bone defect healing with hydroxyapatite coating plasma sprayed on carbon/carbon composite implants. Surf Coat Technol. 2010;205:1150–6.
66. Valerio P, Pereira MM, Goes AM, Leite MF. The effect of ionic products from bioactive glass dissolution on osteoblast proliferation and collagen production. Biomaterial. 2004;25:2941–8.
67. Vitale Brovarone C, Verné E, Appendino P. Macroporous bioactive glass-ceramic scaffolds for tissue engineering. J Mater Sci Mater Med. 2006;17:1069–78.
68. Cuscó R, Guitián F, de Aza S, Artús L. Differentiation between hydroxyapatite and β-tricalcium phosphate by means of μ-Raman spectroscopy. J Eur Ceram Soc. 1998;18:1301–5.
69. Khavryuchenko VD, Khavryuchenko OV, Lisnyak VV. Quantum chemical and spectroscopic analysis of calcium hydroxyapatite and related materials. J Solid State Chem. 2007;180:702–12.

70. Agathopoulos S, Tulyaganov DU, Ventura JMG, Kannan S, Karakassides MA, Ferreira JMF. Formation of hydroxyapatite onto glasses of the CaO–MgO–SiO_2 system with B_2O_3, Na_2O, CaF_2 and P_2O_5 additives. Biomaterial. 2006;27:1832–40.
71. Antonakos A, Liarokapis E, Leventouri T. Micro-Raman and FTIR studies of synthetic and natural apatites. Biomaterial. 2007;28:3043–54.
72. Cerruti M, Bianchi CL, Bonino F, Damin A, Perardi A, Morterra C. Surface modifications of bioglass immersed in TRIS-buffered solution. A multitechnical spectroscopic study. J Phys Chem B. 2005;109:14496–505.
73. Peitl O, Zanotto ED, Hench LL. Highly bioactive P_2O_5–Na_2O–CaO–SiO_2 glass-ceramics. J Non-Cryst Solids. 2001;292:115–26.
74. Price N, Bendall SP, Frondoza C, Jinnah RH, Hungerford DS. Human osteoblast-like cells (MG63) proliferate on a bioactive glass surface. J Biomed Mater Res. 1997;37:394–400.
75. Au AY, Au RY, Demko JL, McLaughlin RM, Eves BE, Frondoza CG. Consil® bioactive glass particles enhance osteoblast proliferation and selectively modulate cell signaling pathways in vitro. J Biomed Mater Res. 2010;94A:380–8.
76. Carinci F, Palmieri A, Martinelli M, Perrotti V, Piattelli A, Brunelli G, Arlotti M, Pezzetti F. Genetic portrait of osteoblast-like cells cultured on perioglas. J Oral Implant. 2007;33:327–33.
77. Anselme K, Sharrock P, Hardouin P, Dard M. In vitro growth of human adult bone-derived cells on hydroxyapatite plasma-sprayed coatings. J Biomed Mater Res. 1997;34:247–59.
78. Yang F, Xie Y, Li H, Tang T, Zhang X, Gan Y, Zheng X, Dai K. Human bone marrow-derived stromal cells cultured with a plasma sprayed CaO–ZrO_2–SiO_2 coating. J Biomed Mater Res B. 2010;95:192–201.
79. Gomes PS, Botelho C, Lopes MA, Santos JD, Fernandes MH. Evaluation of human osteoblastic cell response to plasma-sprayed silicon-substituted hydroxyapatite coatings over titanium substrates. J Biomed Mater Res. 2010;94:337–46.
80. Bhadang KA, Holding CA, Thissen H, McLean KM, Forsythe JS, Haynes DR. Biological responses of human osteoblasts and osteoclasts to flame-sprayed coatings of hydroxyapatite and fluorapatite blends. Acta Biomater. 2010;6:1575–83.
81. Heimann RB. Design of novel plasma sprayed hydroxyapatite-bond coat bioceramic systems. J Therm Spray Technol. 1999;8:597–604.